



<b>Publication Year</b>	2016
<b>Acceptance in OA @INAF</b>	2020-05-04T12:53:46Z
<b>Title</b>	X-ray mirror module analytical design from field of view requirement and stray light tolerances
<b>Authors</b>	SPIGA, Daniele
<b>DOI</b>	10.1117/12.2222907
<b>Handle</b>	<a href="http://hdl.handle.net/20.500.12386/24428">http://hdl.handle.net/20.500.12386/24428</a>
<b>Series</b>	PROCEEDINGS OF SPIE
<b>Number</b>	9905

# X-ray mirror module analytical design from field of view requirement and stray light tolerances

Daniele Spiga<sup>§</sup>

INAF / Brera Astronomical Observatory, Via Bianchi 46, 23807 Merate (Italy)

## ABSTRACT

The design of an X-ray mirror module is a critical issue. In general, the design depends on requirements such as the effective area on-axis, the angular resolution, and the field of view, meant as the angular diameter at which the effective area halves the on-axis one. One has also to come to terms with constraints such as the maximum mass and size allocated in the spacecraft, and the mirror module design consists of fulfilling all these requirements by populating the module with decreasing diameters until the total effective area on-axis is reached without exceeding the mass limit. However, the separation between consecutive shells has to be properly chosen, to avoid excessive obstruction off-axis that would limit the field of view. We already know, in fact, that it is possible to analytically determine a diameter population that is obstruction-free within the field of view. Even though this solution enhances the off-axis effective area, it is not always optimal because it often leaves too much spacing for stray light. The optimal choice for the spacing should hence be the necessary and sufficient one to allow for the required field of view; but, while the computation of the total vignetting from the spacing of mirrors in the module can be done by ray-tracing, the inverse problem is difficult because it should be approached by repeated attempts. Fortunately, the geometric vignetting of a mirror shell can be analytically determined as a function of the off-axis angle and the obstruction parameter, and the expression can be solved for the mirror shell spacing in order to set the field of view to the desired value. In this paper we show how this can be done and how the residual stray light contamination can be computed analytically.

**Keywords:** X-ray mirror module, field of view, optical design, stray light

## 1. INTRODUCTION

Most focusing mirrors for X-ray telescopes have a Wolter-I profile<sup>[1]</sup>, based on two grazing reflections in sequence at the same incidence angle. In grazing incidence, the collecting area of a single X-ray mirror is quite small, therefore a number of confocal mirror is to be nested to fill the mirror module aperture, and the design of an optical module for an X-ray telescope stems from a trade-off among different requirements. The on-axis effective area in a selected X-ray energy band of astrophysical interest is the parameter that most directly affects the telescope sensitivity and is specified since the very first development phases. Operation in space, however, allocates strict limits to the payload and therefore to the maximum size, mass of the module, and telescope focal length: therefore, lightweight materials and thin mirror walls would be desirable in order to reduce mass and on-axis obstruction as much as possible. Nevertheless, integral mirrors in electroformed nickel as of today represent (e.g., Swift/XRT's<sup>[2]</sup> or eROSITA's<sup>[3]</sup>) the most consolidated technique to assemble medium-sized mirror modules with relatively low costs and good angular resolutions. Moreover, the mirror wall thickness cannot be excessively reduced in proportion to the mirror size, if we mean to avert the risk of a mirror deformations and a consequent degradation of the angular resolution on-axis. Also the number and the stiffness of supporting structures, necessary to maintain the mirror shape unchanged through the rigors of launch but unavoidably obstructing the X-ray flux, are to be considered to find the best compromise. Finally, the mirror reflective coating (single, double-, or multi-layer) has to be specifically studied<sup>[4]</sup> to enhance the reflectivity in the range of X-ray energies and incidence angles of interest, but also complex multilayer coatings work efficiently only at shallow incidence angles. Indeed, small incidence angles entail small collecting areas of individual mirrors, and should not thereby be reduced excessively.

The effective area, finally, decreases as an X-ray source moves off-axis, because some rays miss the second reflection and the incidence angles change, with a consequent variation of the total reflectivity. In addition, nested mirror can obstruct each other, and this further reduces the effective area. The decay of the effective area with the off-axis angle determines the *field of view* (FOV) of the mirror module, conventionally defined as the angular diameter where the effective area halves the on-axis value. In a telescope design, the width of FOV is specified by the astronomical targets (e.g., surveys

---

<sup>§</sup> contact author: [daniele.spiga@brera.inaf.it](mailto:daniele.spiga@brera.inaf.it)

or imaging of extended objects), and for wide field telescopes the mirror profile itself<sup>[5]</sup> is specifically designed to ensure little or no degradation of the angular resolution within the FOV. A FOV increase can be naturally obtained reducing the off-axis obstruction, i.e., leaving additional spacing between mirror shells. In fact, to avoid on-axis obstruction one just needs the *inner* median (i.e., at the primary-secondary intersection) radius  $R_0$  of each mirror shell to be larger than the maximum radius  $R_M^*$  of the next smaller shell (Fig. 1). Designing a mirror module with such tight nesting would maximize the on-axis area, but would make the off-axis vignetting too severe. Finding the optimal angular spacing usually entails a number of ray-tracing attempts, which are time consuming especially if many different configurations have to be tested.

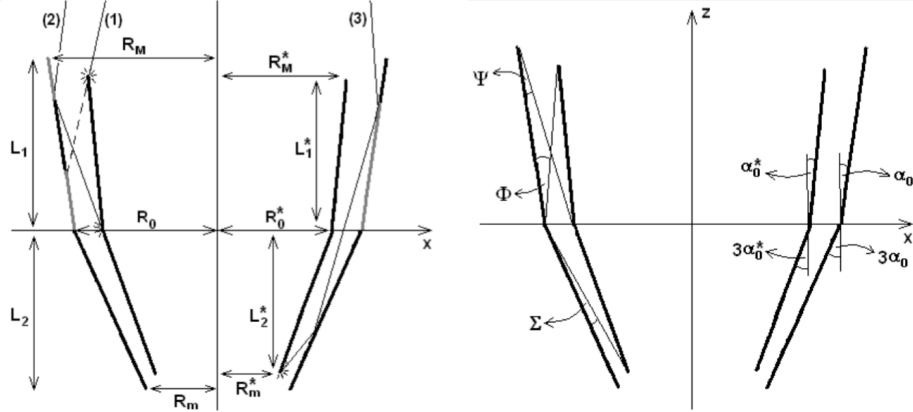


Fig. 1: (left) a meridional section of a pair of nested Wolter-I mirror shells with a common primary-secondary intersection plane. The main dimensional parameters are indicated. Also drawn are the three possible effective area obstructions of the outer mirror shell by the next inner one. (right) The three obstruction angles,  $\Phi$ ,  $\Psi$ ,  $\Sigma$  that rule the three species of obstruction.

In order to speed up the mirror module design, analytical methods have been developed to perform the computation of the off-axis effective area<sup>[6]</sup>, and also accounting for mutual mirror obstruction<sup>[7]</sup>. One of the results is that the obstruction off-axis of a Wolter-I mirror shell (including the self-vignetting for double reflection) depends solely on the incidence angles on the primary and the secondary segment of the mirror,  $\alpha_1$  and  $\alpha_2$ , and on three obstruction angles  $\Phi$ ,  $\Psi$ ,  $\Sigma$  that are characteristic of the spacing of the nested mirror shell pair (Fig. 1). Based on these results, it is possible to derive conditions for mirror pairs to be completely obstruction-free up to a given off-axis angle  $\theta_f$ . Selecting then  $\theta_f = \frac{1}{2}$  FOV, the conditions can be applied recursively to obtain a mirror module design that maximizes the effective area within the FOV.

In some cases, however, the mirror design mentioned above might be inappropriate. Firstly, not all the telescope projects require a wide FOV. Secondly, usually the required FOV can be obtained also in presence of a moderate obstruction off-axis. Thirdly, the obstruction in a nested mirror module also plays an important role in the suppression of *stray light*, i.e., rays that make a single reflection and, though unfocused, represent a major source of background and image ghosts when a bright X-ray source is outside the field of view of the telescope<sup>[8]</sup>. In fact, a loose nesting often leaves too much room for stray rays to propagate throughout the mirror module. For example, Fig. 2 displays the trend of geometric area for double reflection (focused), stray light from the primary segments (SL1) and secondary (SL2) in a shell pair with a loose (left) and a tight (right) mirror spacing, as a function of the off-axis angle  $\theta$ . The curves were traced using analytical formulae, derived in a previous paper<sup>[8]</sup>, which return the geometric area as a function of  $\theta$ , normalized to the geometric area on-axis. We notice that a tighter design (Fig. 2, right) yields a focused geometric area that drops quite rapidly off, with a FOV of nearly 7 arcmin, vs. a 12 arcmin allowed by a more relaxed spacing between shells (Fig. 2, left). However, in the latter case the total geometric area for stray light is *ten times higher*, which is potentially harmful.

Even if X-ray baffles are frequently used to reduce the impact of the stray light, it might be convenient to start from a mirror module design that ensures the desired FOV for focused X-rays but, at the same time, minimizes the effective area for stray light: this is equivalent to finding the mirror spacing *necessary and sufficient* to return the required FOV. Finding the optimal spacing of every single mirror shell by iterated ray-tracing attempts would be, however, a too lengthy task. In contrast, approaching the problem using the analytical formulae that express the geometric area, as a function of the off-axis angle, would allow a faster design of a Wolter-I module. The only approximation is that the formalism is based on the geometric area instead of the effective area, i.e., it does not account for the variation of coating reflectivity with the incidence angles, which also change when varying  $\theta$ . Hence, the efficiency of the final design will have to be checked using the direct computation of the effective area<sup>[7]</sup>.

In this paper we show how the formalism for the geometric area variation can be inverted (Sect. 2) to return the value of  $\theta$  that halves the on-axis geometric area. We see that this cannot be exactly done analytically, but the problem can be faced by iterated approximations, at least in a broad range of incidence angles. We show in Sect. 3 an example of application to the design of a Wolter-I mirror module, and the design verification using the analytical formulae for the effective area<sup>[7]</sup> and for stray light contamination<sup>[8]</sup>. Finally, we briefly recapitulate the results in Sect. 4.

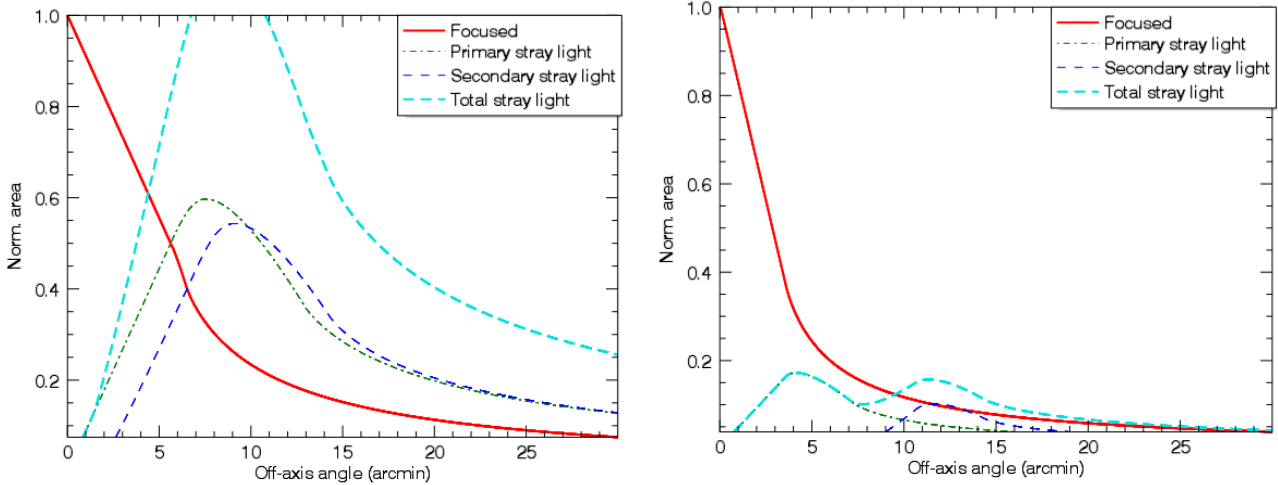


Fig. 2: computation of the normalized geometric area for double reflection, and for total stray light, in a Wolter-I mirror shell with  $f = 12$  m,  $R_0 = 100$  mm,  $L = 300$  mm. The inner mirror shell has the same length and focal, but an outer radius at the I.P. of (left)  $R_0^* = 98.95$  mm and (right)  $R_0^* = 99.38$  mm. In the first case, the larger field of view is paid with a higher intensity of the stray light.

## 2. INVERSION OF THE GEOMETRIC AREA FUNCTION

A detailed description of the formalism for the off-axis effective area is out of the scope of this paper. We just recall here the most relevant results, reported in detail elsewhere<sup>[7]</sup>. Let us consider a single shell, solely obstructed by the adjacently inner shell with *outer* (i.e., of the non-reflective surface) radius at the intersection plane  $R_0^*$ , as displayed in Fig. 1. We assume the two shells to have the same intersection plane. If the focal length is much larger than the mirror length - a condition usually well fulfilled in real cases - the Wolter-I profile can be approximated by a double cone as long as the effective area is concerned. Under these hypotheses, the effective area of the mirror shell is expressed by the formula<sup>[7]</sup>

$$A(\lambda, \theta) = \int_0^\pi [(L\alpha)_{\min} - Q_{\max}]_{\geq 0} r_\lambda(\alpha_1) r_\lambda(\alpha_2) d\varphi, \quad (1)$$

where the  $[\ ]_{\geq 0}$  brackets mean that the enclosed expression has to be set to zero when negative. The quantities appearing in the integrand are related to the obstruction parameters  $\Phi$ ,  $\Psi$ ,  $\Sigma$  (see Fig. 1) and the incidence angles  $\alpha_1$ ,  $\alpha_2$ ,

$$(L\alpha)_{\min} = \min(L_1\alpha_1, L_2\alpha_2, L_1\Psi), \quad (2)$$

$$Q_{\max} = \max[L_1^*(\alpha_1 - \Phi), L_2^*(\alpha_2 - \Sigma), 0]. \quad (3)$$

The incidence angles functions of the polar angle  $\varphi$  in the  $xy$  plane; in the astronomical case the X-ray source is virtually located at infinity, so they have the simplified expressions:

$$\alpha_1(\varphi) = \alpha_0 - \theta \cos \varphi, \quad (4)$$

$$\alpha_2(\varphi) = \alpha_0 + \theta \cos \varphi, \quad (5)$$

where  $\alpha_0 \approx R_0/4f$  is the incidence angle on-axis. In the following we consider only the frequent case that  $L_1 = L_2$ , omitting the subscript. For sufficiently long focal lengths ( $f \gg L$ ) we can also assume that

$$\Phi \approx \Sigma \approx \Psi = \frac{R_0 - R_0^*}{L}, \quad (6)$$

and adopt  $\Phi$  as the unique obstruction parameter expressing the angular spacing of shells. Now, for values of the off-axis angle  $\theta < \Phi - \alpha_0$ , the reflective shell is not obstructed and the off-axis geometric area, normalized to the on-axis one, is given by the formula<sup>[6]</sup>:

$$\frac{A_\infty(\theta)}{A_\infty(0)} = 1 - \frac{2\theta}{\pi\alpha_0}. \quad (7)$$

The field of view,  $F$ , can be defined as twice the off-axis angle,  $\theta_F$ , at which

$$A_\infty(\theta_F) = \frac{1}{2}A_\infty(0), \quad (8)$$

now, since we are assuming the mirror to be *deliberately* obstructed to reduce the stray light, we also suppose that the effective area is halved at off-axis angles larger than  $\Phi - \alpha_0$ , where the focused area decrease is caused not only by the mirror self-vignetting, but also by the mirror obstruction. When this occurs, i.e., for  $\Phi - \alpha_0 < \theta < \Phi$ , the off-axis geometric area is well expressed by<sup>[7]</sup>

$$\frac{A_\infty(\theta)}{A_\infty(0)} = 1 - \frac{2\theta}{\pi\alpha_0} \left[ 1 + S\left(\frac{\Phi - \alpha_0}{\theta}\right) \right], \quad (9)$$

where  $S(x)$  is a function defined as

$$S(x) = \int_x^1 \arccos w \, dw = \sqrt{1-x^2} - x \arccos x. \quad (10)$$

Comparing Eqs. 8 and 9 we obtain

$$S\left(\frac{\Phi - \alpha_0}{\theta_F}\right) = \frac{\pi\alpha_0}{4\theta_F} - 1 : \quad (11)$$

solving this equation for  $\Phi$  provides the design with the required geometric FOV,  $F$ . Because the  $S(x)$  function takes on values between 0 and 1, the last equation has a solution only if  $1 < \pi\alpha_0/4\theta_F < 2$ , i.e., only if

$$\frac{2}{\pi}F < \alpha_0 < \frac{4}{\pi}F, \quad (12)$$

for all the mirror shells in the optical module. Setting  $u = \pi\alpha_0/4\theta_F - 1$  (hence,  $0 < u < 1$ ) and  $x = (\Phi - \alpha_0)/\theta_F$ , Eq. 11 takes the convenient form

$$\sqrt{1-x^2} = x \arccos x + u, \quad (13)$$

and this equation can be solved by a succession of approximated values  $x_0, x_1, x_2, \dots$  (Fig. 3), provided, e.g., by the recursive solution of the equation array

$$\begin{cases} y_{n+1} = 3(x_{n+1} - x_n) + x_n \arccos x_n + u \\ y_{n+1} = \sqrt{1-x_{n+1}^2} \end{cases}, \quad (14)$$

that is, setting  $y_{n+1} - 3x_{n+1} = t_{n+1}$  and solving the second equation for  $x_{n+1}$ ,

$$\begin{cases} t_{n+1} = x_n(\arccos x_n - 3) + u \\ x_{n+1} = \frac{\sqrt{10 - t_{n+1}^2} - 3t_{n+1}}{10} \end{cases}, \quad (15)$$

starting from  $x_0 = 0$ . An example is given in Fig. 3: the  $x_n$  succession converges to a limit value  $x$ , and hence a value of  $\Phi$ , for every value of  $\alpha_0$  fulfilling the conditions in Eq. 12. Once found a value for  $\Phi$ , we use Eq. 6 to determine the value of  $R_0^*$ , and therefore, after subtracting the mirror thickness, the  $R_0$  value for the next mirror shell.

The procedure from Eq. 11 is repeated for the next shell using the new value of  $R_0$ , and so on until the on-axis effective area of the mirror module reaches the desired value. The sequence of  $R_0$  values provides the required design.

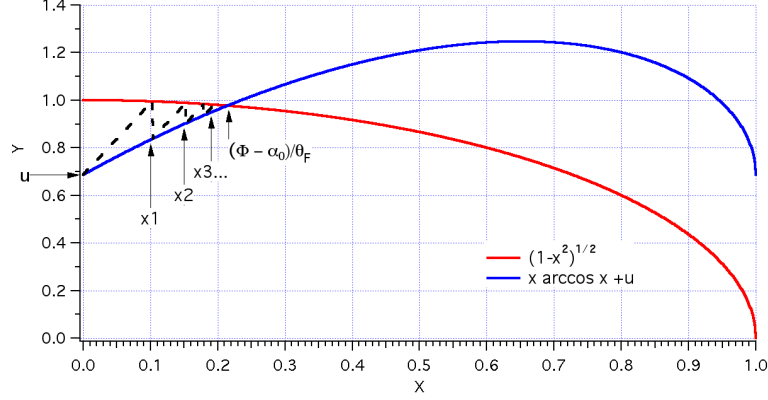


Fig. 3: numerical solution of Eq. 13. The specification of the field of view (via the  $u$  parameter) allows us finding the optimal  $\Phi$  parameter corresponding to  $\alpha_0$ , i.e., for every pair of adjacent shells. The dashed tilted lines represent the iterative application of Eqs. 15. The vertical lines locate the  $x_0, x_1, x_2, \dots$  succession converging to the intersection of the two curves.

### 3. AN EXAMPLE OF MIRROR MODULE DESIGN

In this section we show an example of application of the method described in the previous section. To this end, we compare two possible optical designs, both consisting of 28 mirror shells with a 10 m focal length and a maximum 250 mm diameter at the intersection plane. The mirror wall thickness is supposed to be variable throughout the module, i.e.,  $1.75 \times 10^{-3}$  times the shell radius as done in the development of the NHXM project<sup>[9]</sup> to ensure a mirror stiffness compatible with a 20 arcsec HEW angular resolution, with a minimum thickness value of 0.2 mm. Both primary and secondary mirror segments have a fixed length  $L = 300$  mm, and a 10% obstruction by the supporting spiders is assumed. Finally, we request a 10 arcmin FOV; we therefore have two choices for the spacing between consecutive shells, which entail two different designs:

1. “Loose” design: the angular spacing between shells is selected to avoid any obstruction up to an off-axis angle of 5 arcmin. To fulfill this criterion, the mirror module is populated as described in<sup>[7]</sup>. In this design (Fig. 4, triangles), the FOV is interpreted as the unobstructed field: the real FOV (meant at the 50% vignetting function) will in general be broader than 10 arcmin, but at the same time we run the risk to funnel too much stray light in the gaps between shells (Fig. 5, left). The total, on-axis geometric area of the module equals  $131.6 \text{ cm}^2$  and the total mirror mass turns out to be 20 kg.
2. “Tight” design: the angular spacing is determined by the aim of returning a 10 arcmin geometric FOV, following the method described in Sect. 2. The mirror shells are nested more densely (Fig. 4, circles) than in the loose design, but the distance is exactly as needed to ensure the required FOV, at least geometrically. The reduced spacing takes the advantage to better obstruct the stray light (Fig. 5, right). With this approach, the total, on-axis geometric area of the module is  $142 \text{ cm}^2$  with a total mirror mass of 21 kg. The on-axis performances of the two solutions are thereby more or less equivalent.

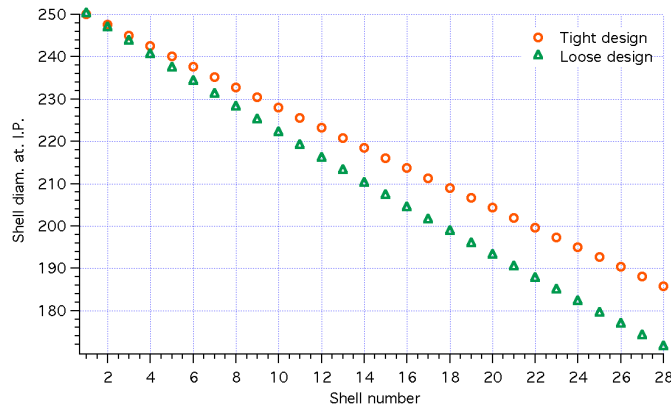


Fig. 4: diameter successions as a function of the shell number for a mirror module with  $f = 10$  m, maximum  $2R_0 = 250$  mm, and  $L_1 = L_2 = 300$  mm. Triangles: loose nesting with 10 arcmin of unobstructed FOV. Circles: tight nesting with a 10 arcmin geometric FOV.

The performance verification in terms of effective area is reported in detail in the next subsections. However, a simple geometric computation already shows that the second design is much more effective. In Fig. 5 we have computed the total geometric vignetting (thick, solid lines) for the two solutions found: we notice that the tight design (right viewgraph) halves the vignetting function at an off-axis angle of 5 arcmin and thereby returns the required 10 arcmin FOV. In the same figure, we have also displayed the total geometric effective area for stray light, integrated over the entire focal plane, computed using the analytical formulae<sup>[8]</sup> for the geometric area of SL1 and SL2. The much lower intensity of the stray light in the tight design, and the consequent benefit on the background, is apparent. In reality, this computation accounts neither for the mirror reflectivity, nor for the finite size of the detector. To perform a more accurate assessment we have to adapt the formalism for the focused effective area<sup>[7]</sup> and for the stray light.<sup>[8]</sup> This is done in the next subsections.

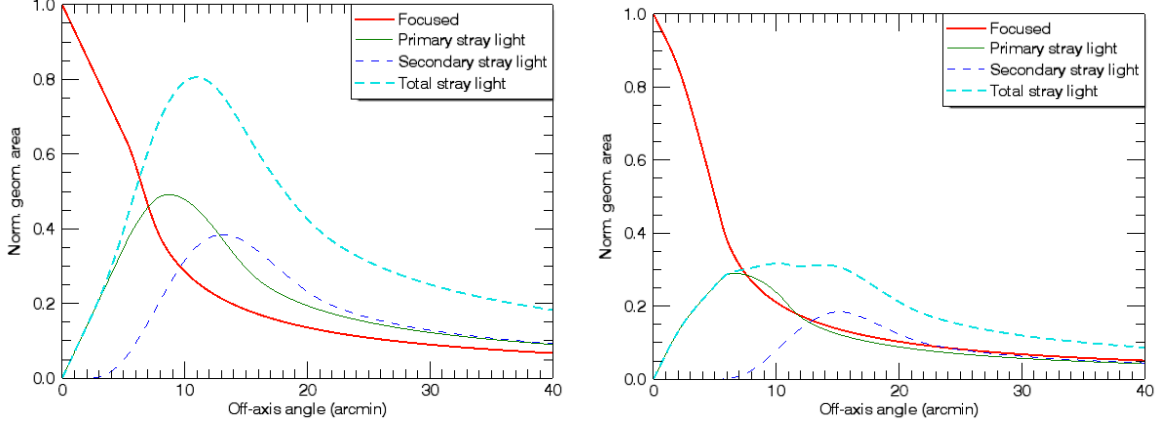


Fig. 5: geometric area for double reflection and stray light using (left) the loose design and (right) the tight design of the mirror module. We note the much lesser impact of the stray light in the second case, which still guarantees a 10 arcmin diameter FOV.

### 3.1. Effective area vignetting

In order to determine the different vignetting functions in the two designs, we have adapted the computation of the off-axis effective area for double reflection, accounting for mutual shell obstruction<sup>[7]</sup> and for spider obstruction<sup>[8]</sup>. In the original papers, integral formulae for the effective area at a fixed off-axis angle  $\theta$ , as a function of  $\lambda$ , were provided. Here we are, however, more interested in estimating the effective area for stray light as a function of the off-axis angle  $\theta$  at fixed  $\lambda$ . To do this, we might in principle repeat the computation for each value of  $\theta$ , which is quite ineffective. Hence, we prefer writing the expression of the effective area dependence on  $\theta$ , at a fixed value of  $\lambda$ .

We can start from the expression reported in a previous paper, valid for i) an *unobstructed* mirror shell and ii) illuminated by a source at infinity.<sup>[10]</sup>

$$A(\lambda, \theta) = 4R_0L \int_{\alpha_0-\theta}^{\alpha_0} \frac{\alpha_1}{\sqrt{\theta^2 - (\alpha_1 - \alpha_0)^2}} r_\lambda(\alpha_1)r_\lambda(\alpha_2)d\alpha_1, \quad (16)$$

in which the integration is performed on  $\alpha_1$  instead of the polar angle  $\varphi$  (mutually related by Eq. 4), and omitting the  $\infty$  subscript to simplify the notation. Equation 16 is derived under the hypothesis that the contribution to the effective area is the same in the four quadrants of the  $xy$  plane, which is true in the hypotheses i) and ii) mentioned above, and this is the reason of the 4 factor appearing therein. We have therefore taken four times the contribution of the 1<sup>st</sup> quadrant, in which Eq. 2 simply reduces to  $L\alpha_1$ . In presence of obstruction, in contrast, the symmetry is partially lost because the obstruction in the 1<sup>st</sup> quadrant is determined by  $\Sigma$ , while it depends on  $\Phi$  in the 2<sup>nd</sup> quadrant (in the 4<sup>th</sup> and the 3<sup>rd</sup> quadrant is the same as the 1<sup>st</sup> and the 2<sup>nd</sup> respectively). We assume  $\Psi$  to be irrelevant because the primary and the secondary segment have the same length  $L$  and  $\alpha_0 < \Psi$  for all the shells. Separating the contributions of the right quadrants (where  $\min(\alpha_1, \alpha_2) = \alpha_1$ ) and those in the left quadrants (where  $\min(\alpha_1, \alpha_2) = \alpha_2$ ), we can modify Eq. 16 accounting for the obstruction (Eq. 1):

$$A(\lambda, \theta) = 2R_0L \left\{ \int_{\alpha_0-\theta}^{\alpha_0} \frac{[\alpha_1 - [\alpha_2 - \Sigma]_{\geq 0}]_{\geq 0}}{\sqrt{\theta^2 - (\alpha_1 - \alpha_0)^2}} r_\lambda(\alpha_1)r_\lambda(\alpha_2)d\alpha_1 + \int_{\alpha_0-\theta}^{\alpha_0} \frac{[\alpha_2 - [\alpha_1 - \Phi]_{\geq 0}]_{\geq 0}}{\sqrt{\theta^2 - (\alpha_2 - \alpha_0)^2}} r_\lambda(\alpha_1)r_\lambda(\alpha_2)d\alpha_2 \right\} \quad (17)$$

and, using the relation  $\alpha_2 = 2\alpha_0 - \alpha_1$  (Eqs. 4 and 5) to change the integration variable, we conveniently rewrite Eq. 17 as

$$A(\lambda, \theta) = 2R_0L \left\{ \int_{\alpha_0-\theta}^{\alpha_0} \frac{[\alpha_1 - [\alpha_2 - \Sigma]_{\geq 0}]_{\geq 0}}{\sqrt{\theta^2 - (\alpha_1 - \alpha_0)^2}} r_\lambda(\alpha_1) r_\lambda(\alpha_2) d\alpha_1 + \int_{\alpha_0}^{\alpha_0+\theta} \frac{[\alpha_1 - [\alpha_2 - \Phi]_{\geq 0}]_{\geq 0}}{\sqrt{\theta^2 - (\alpha_0 - \alpha_1)^2}} r_\lambda(\alpha_1) r_\lambda(\alpha_2) d\alpha_1 \right\} \quad (18)$$

where the first term takes contributions from the *right* quadrants and the second one from the *left* quadrants. We note that the sole factors depending on  $\lambda$  are the reflectivities, while the remaining factors are purely geometric. Hence, the average area over a wavelength band  $\Delta\lambda$  is simply obtained replacing the reflectivity product in Eq. 18 with its average over  $\Delta\lambda$ . The obstruction from the spider is almost constant for such small off-axis angles, and can be accounted for in the computation by removing from the integration set the angular values occupied by the spider spokes. Finally, we notice that no limitation by the detector size is assumed, because we can reasonably suppose that the focal spot is always entirely enclosed in the detector area.

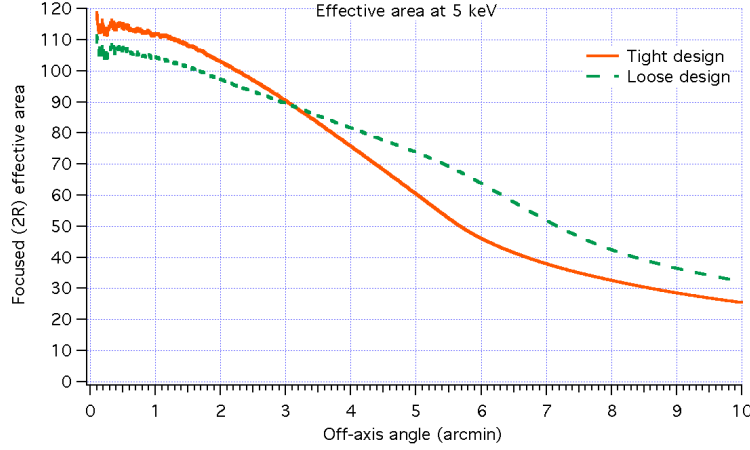


Fig. 6: total effective area at the test energy of 5 keV, assuming a 30 nm gold coating of the mirrors, as a function of the off-axis angle, for the tight and the loose design cases.

Application of Eq. 18 at 5 keV to the two test designs returns the results reported in Fig.6. We note that the tight design, in addition to a higher effective area on-axis, returns exactly a 10 arcmin FOV as initially requested. The loose design is characterized by a larger FOV: however, as we see in the next subsection, the loose design is more affected by stray light contamination in the field of view of the telescope.

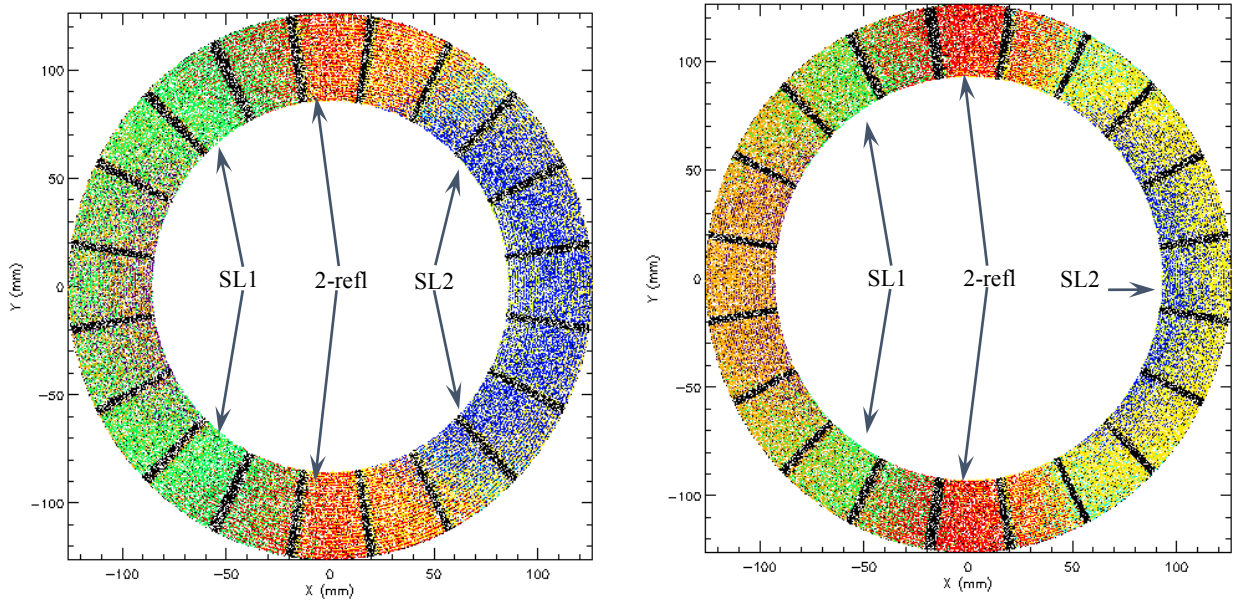


Fig. 7: ray-tracing results at 5 keV for the (left) loose and the (right) tight design, for a point-like source, 12 arcmin off-axis. The colors refer to different destinies of rays. The origin points of SL1 are green and those of SL2 are blue. Yellow and orange ones are obstructed; red dots correspond to a double reflection. We notice the larger suppression of stray rays in the tighter mirror module design.

### 3.2. Detailed computation for stray light

We can now compare the different stray light amount in the two mirror module designs. An analytical formalism for the effective area of the primary (SL1) and the secondary (SL2) stray light as a function of  $\lambda$ , at fixed  $\theta$ , has already been described in another paper<sup>[8]</sup>. To obtain an expression as a function of  $\theta$ , we can repeat the same passages to Eq. 18, but keeping in mind some differences:

- i) stray light stems from singly-reflected rays and is not focused, but typically forms arcs of variable shape and size, also well described by known analytical expressions;<sup>[7],[8]</sup> hence, the amount of detected stray light from a source off-axis is limited by the detector area. In this work we consider a detector in fixed position, centered on-axis, therefore the really detected stray light (unlike the total, geometric stray light reported in Fig. 5) appears only when  $\theta$  reaches a threshold value that chiefly depends on the detector size.
- ii) as the X-ray source is at infinity as in our case, SL1 can only arise from single reflection in the *left* quadrants of the  $xy$  plane, while SL2 may only result from single reflections in the *right* quadrants of the entrance pupil (Fig. 7).

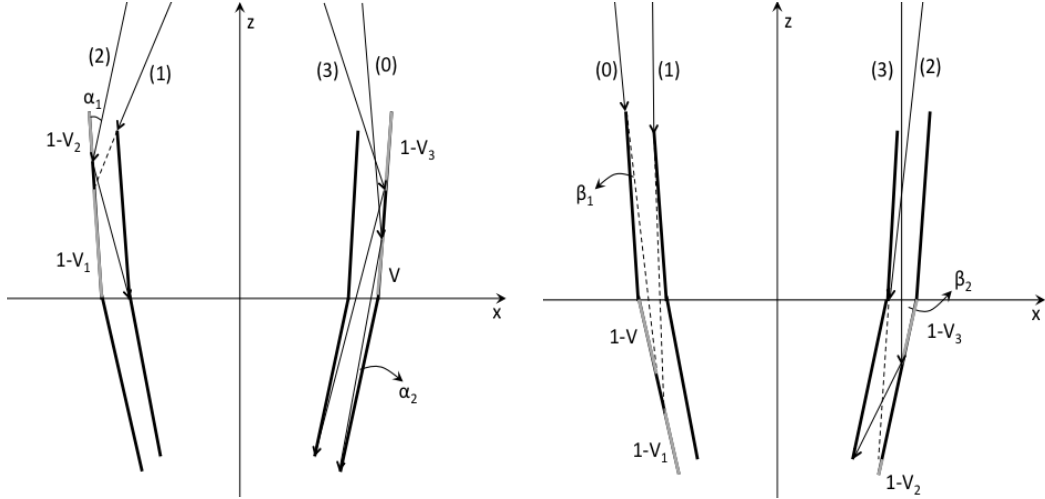


Fig. 8: (left) possible sources of obstruction of primary stray light. (right) possible sources of obstruction of secondary stray light. The meaning of the  $\alpha_1$ ,  $\alpha_2$ ,  $\beta_1$ , and  $\beta_2$  angles is also shown.

For SL1, the correct expression is obtained modifying the second term of Eq. 18, after removing the second reflection and accounting for all the possible sources of vignetting (see Fig. 8, left, and details in<sup>[8]</sup>):

$$A_{\infty}^{SL1}(\lambda, \theta) = 2R_0L \int_{\alpha_0}^{\alpha_0+\theta} \frac{[\min(\alpha_1, \Psi, \Sigma + \alpha_2) - [\max(\alpha_2, \alpha_1 - \Phi)]_{\geq 0}]_{\geq 0}}{\sqrt{\theta^2 - (\alpha_1 - \alpha_0)^2}} \chi_P(\alpha_1) r_{\lambda}(\alpha_1) d\alpha_1. \quad (19)$$

In Eq. 19 the  $[\ ]_{\geq 0}$  brackets mean, as usual, that the enclosed expression has to be set to zero when negative. We have also limited the integration set to the interval of incidence angles  $P$  that reflect rays within the detector area - a square of side  $d$  - by adding the factor  $\chi_P(\alpha_1)$ , the characteristic function of the  $P$  set, which can be easily computed using the parametric expressions of the SL1 pattern<sup>[7],[8]</sup>, in the simplified case of a source at infinity and at the nominal focal plane:

$$x_1(\varphi) = (R_0 - 2\alpha_0 f) \cos \varphi + \theta f \cos 2\varphi, \quad (20)$$

$$y_1(\varphi) = (R_0 - 2\alpha_0 f) \sin \varphi + \theta f \sin 2\varphi. \quad (21)$$

Since the detector is centered on-axis, the  $P$  interval is defined by the condition

$$\min[|x_1(\alpha_1)|, |y_1(\alpha_1)|] \leq d/2, \quad (22)$$

where the polar angles have been replaced with  $\alpha_1$ , using Eq. 4. This function can also be modified to exclude the polar angles obstructed by the spider at the entrance and the exit pupil.

To compute SL2, we modify the first term of Eq. 18 replacing  $\alpha_0$  with  $3\alpha_0$  and  $\alpha_1$  with  $\beta_2$ , the direct incidence angle on the secondary segment (Fig. 8, right),

$$\beta_2(\varphi) = 3\alpha_0 - \theta \cos \varphi, \quad (23)$$

$$\beta_1(\varphi) = \theta \cos \varphi - \alpha_0. \quad (24)$$

and accounting for all the possible sources of obstruction (see Fig. 8, right, and details in<sup>[8]</sup>) we obtain:

$$A_{\infty}^{SL2}(\lambda, \theta) = 2R_0L \int_{3\alpha_0-\theta}^{3\alpha_0} \frac{[\min(\beta_2, \Psi, \beta_1 + \Phi) - [\max(\beta_1, \beta_2 - \Sigma)]_{\geq 0}]_{\geq 0}}{\sqrt{\theta^2 - (\beta_2 - 3\alpha_0)^2}} \chi_P(\beta_2) r_{\lambda}(\beta_2) d\beta_2. \quad (25)$$

where the  $\chi_P(\beta_2)$  is the characteristic function of the P set, still defined as the interval of incidence angles on the secondary segment for which the stray light pattern described by the parametric functions

$$x_2(\varphi) = (R_0 - 6\alpha_0 f) \cos \varphi + \theta f \cos 2\varphi, \quad (26)$$

$$y_2(\varphi) = (R_0 - 6\alpha_0 f) \sin \varphi + \theta f \sin 2\varphi \quad (27)$$

fulfills the condition

$$\min[|x_2(\beta_2)|, |y_2(\beta_2)|] \leq d/2. \quad (28)$$

Just like SL1, we can also exclude from the P set the angular regions occupied by the spiders.

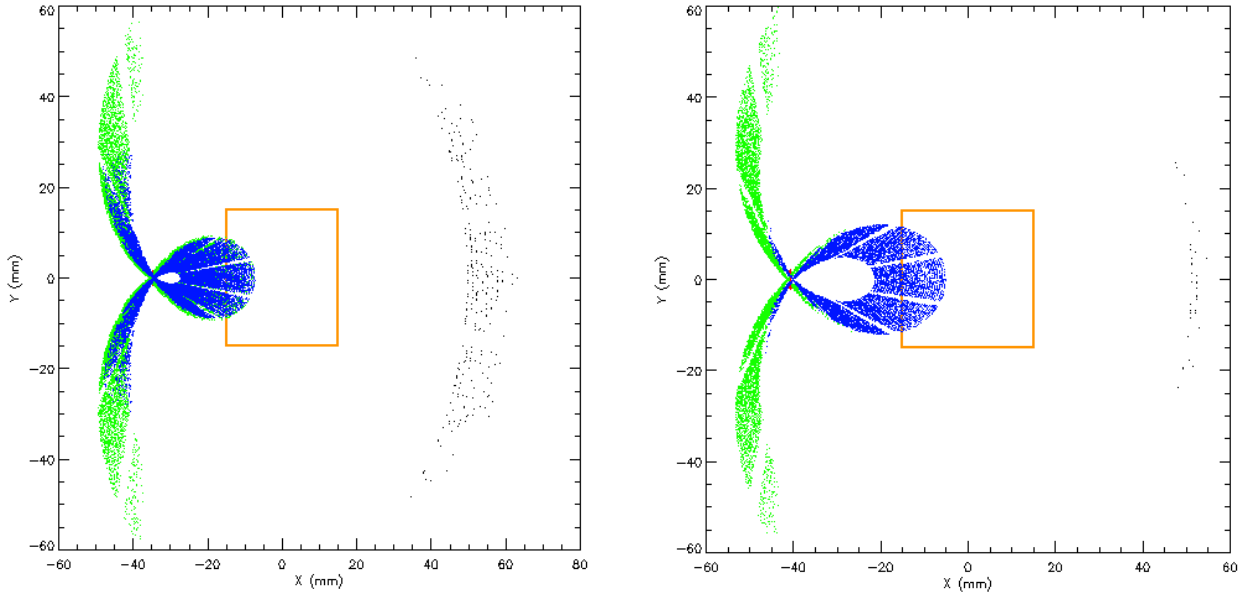


Fig. 9: final ray positions on the focal plane out of the ray-tracing at 5 keV for the loose (left) and the tight design (right), assuming a point-like source, 12 arcmin off-axis, at 5 keV. The rectangle represents the detector area. Green dots denote SL1, blue dots represent SL2. The black dots on the right side of the two images are rays directly passing through the module.

We now compute the total stray light at 5 keV, as a function of the off-axis angle, in the two designs of the mirror module under analysis in this section. We therefore applied Eqs. 19 and 25 shell by shell, and summed all the stray light contributions (SL1+SL2). Moreover, we validated the model using a ray-tracing routine applied to the same mirror module designs. In Fig. 7 we show the mirror module apertures illuminated by a source at 5 keV, off-axis by 12 arcmin, and marking the entrance position of each ray in a different colour, depending on the ray destiny. We note that in the loose design the area giving rise to stray light (green and blue) is much larger than in the tight design, which is much more obstructed as desired. Figure 9 displays the final positions of the rays on the focal plane.

The results of the analytical computation are in perfect agreement with the ray-tracing findings (Fig. 10). The analytical method, however, takes the advantages of a i) simpler implementation, ii) a much shorter computation time, iii) no statistical uncertainties, and iv) a much higher resolution in the off-axis angle scale.

The simulations in Fig. 10, in addition to validating the analytical model, shows that the tight design effectively attenuates the stray light in the detector area, at least at off-axis angle values below 16 arcmin. Moreover, in the loose

design we have a contribution of SL1 at off-axis angles below 14 arcmin, which is completely suppressed in the tight design. This is an important point because a pre-collimator in front of the optical module can easily reduce the secondary stray light, but it is ineffective at blocking the primary one.<sup>[1]</sup> Therefore, the adoption of a mirror spacing tuned to return exactly a given FOV can improve the efficiency of an X-ray baffle and reduce the contamination of stray-light within the detector area.

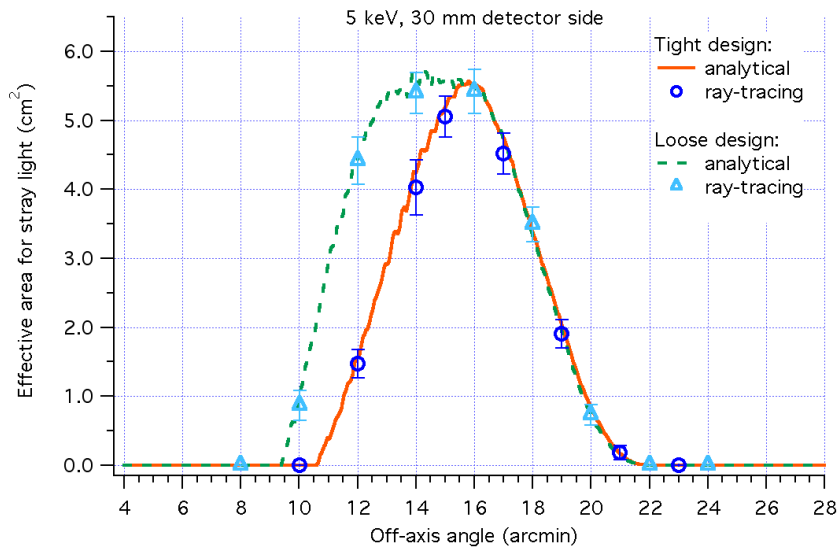


Fig. 10: computed effective area for stray light at 5 keV for the tight and the loose design, as a function of the off-axis angle. The analytical computation (lines) shows that adopting the “tight” design, aiming at a 10 arcmin imaged FOV (Sect. 2), the stray light is attenuated at off-axis angles below 16 arcmin with respect to a “loose” design aimed at simply avoiding obstruction within the FOV. The ray-tracing results (symbols) perfectly validate the analytical method predictions.

#### 4. CONCLUSIONS

In this work we have exposed a new method to design an X-ray telescope mirror module, entirely based on analytical formulae, in order to exactly fulfill the requirements on the field of view and, at the same time, to minimize the stray light contamination on the focal plane. This is obtained setting the spacing between nested shell pairs to the necessary and sufficient value to limit the 50% vignetting function to the required FOV. The correct spacing can be determined inverting numerically an existing formalism to compute the obstruction of the effective area. In this way, we can increase the obstruction of the stray light out of the optical module and reduce the formation of ghosts on the focal plane, increasing the efficiency of an X-ray pre-collimator that could be used to suppress the remaining stray light. We have shown this through an example, which also gave us the opportunity to derive useful formulae to evaluate the stray light intensity in the detector area.

#### ACKNOWLEDGMENTS

The author thanks F. Muleri, P. Soffitta (INAF/IAPS Roma), G. Tagliaferri, S. Campana, K. Tayabaly, J. Holyszko, and especially B. Salmaso (INAF/OAB) for profitable discussions.

#### REFERENCES

- [1]. Van Speybroeck, L. P., Chase, R. C., “Design parameters of paraboloid-hyperboloid telescopes for X-ray astronomy,” *Applied Optics* 11(2), 440 (1972)
- [2]. Citterio, O., Conconi, P., Ghigo, M., Loi, R., Mazzoleni, F., Poretti, E., Conti, G., Mineo, T., Sacco, B., Bräuninger, H., Burkert, W., “X-Ray optics for the JET-X experiment aboard the SPECTRUM-X Satellite,” *Proc. SPIE* 2279, 480 (1994)
- [3]. Friedrich, P., Bräuninger, H., Budau, B., Burkert, W., Burwitz, V., Dennerl, K., Eder, J., Freyberg, M., Gaida, R., Hartner, G., Menz, B., Pfeffermann, E., Predehl, P., Rohé, C., Schreib, R., “Development and testing of the eROSITA mirror modules,” *Proc. SPIE* 8443, 84431S (2012)

- [4]. Cotroneo, V., Pareschi, G., Spiga, D., Tagliaferri, G., "Optimization of the reflecting coatings for the New Hard X-ray Mission," Proc. SPIE 7437, 743717 (2009)
- [5]. Conconi, P., Campana, S., Tagliaferri, G., et al. "A wide field X-ray telescope for astronomical survey purposes: from theory to practice," Monthly Notices of the Royal Astronomical Society 405, 877 (2010)
- [6]. Spiga, D., Cotroneo, V., Basso, S., Conconi, P., "Analytical computation of the off-axis effective area of grazing incidence X-ray mirrors," Astronomy & Astrophysics 505, 373 (2009)
- [7]. Spiga, D., "Optics for X-ray telescopes: analytical treatment of the off-axis effective area of mirrors in optical modules," Astronomy & Astrophysics 529, A18 (2011)
- [8]. Spiga, D., "Analytical computation of stray light in nested mirror modules for X-ray telescopes," Proc. SPIE 9603, 96030H (2015)
- [9]. Basso, S., Pareschi, G., Citterio, O., Spiga, D., Tagliaferri, G., Raimondi, L., et al., "The optics system of NHXM: status report," Proc. SPIE 8147, 814709 (2011)
- [10]. Spiga, D., Cotroneo, V., "Computation of the off-axis effective area of the New Hard X-ray Mission modules by means of an analytical approach," Proc. SPIE 7732, 77322K (2010)
- [11]. Cusumano, G., Artale, M., Mineo, T., Teresi, V., Pareschi, G., Cotroneo, V., "Simbol-X: x-ray baffle for straylight reduction," Proc. SPIE 6688, 66880C (2007)